Article

Mathematical Modeling of Efficiency Evaluation of Double-Pass Parallel Flow Solar Air Heater

Varun Pratap Singh [1,*], Siddharth Jain [1], Ashish Karn [1], Ashwani Kumar [2], Gaurav Dwivedi [3], Chandan Swaroop Meena [4,*] and Raffaello Cozzolino [5,*]

1   Department of Mechanical Engineering, School of Engineering, University of Petroleum and Energy Studies India, Dehradun 248007, India
2   Technical Education Department Uttar Pradesh, Kanpur 208024, India
3   Energy Centre, Maulana Azad National Institute of Technology, Bhopal 462003, India
4   CSIR—Central Building Research Institute, Roorkee 247667, India
5   Department of Engineering, University of Rome Niccolò Cusano, 00166 Roma, Italy
*   Correspondence: ray_varun@yahoo.com (V.P.S.); chandanswaroop2008@gmail.com (C.S.M.); raffaello.cozzolino@unicusano.it (R.C.)

Abstract: To investigate the influencing range and optimize values of different operational and system parameters on the double-pass parallel flow solar air heater's (DPPFSAH) thermal, effective, and exergetic efficiencies, an iterative method was used to analyze the governing energy equations using a theoretical model written in MATLAB based on the Nusselt number (Nu) and friction factor (f) correlations developed in the work performed earlier. A comparison between double-pass and single-pass SAHs for mathematical and experimental outcomes was conducted, and the results were found to be fairly consistent. According to the thermo-hydraulic performance indicators, similar to single-pass SAHs, perforated multi-V rib-roughened DPPFSAHs achieve optimum thermal performance for lower Reynolds numbers, which does not change much as the Reynolds number increases above 18,000. This finding can be taken into account when designing any DPPFSAH.

Keywords: solar energy; solar air heater; mathematical modelling; parameter optimization; double pass

1. Introduction

Because of its simplistic design, simple operation, easy maintenance, and low initial investment, a solar collector for air heating is particularly beneficial for applications requiring low thermal energy. The heat a working fluid absorbs from a solar collector determines how well the collector performs. By raising the heat transfer coefficient (h) or the heat transfer surface area in between the absorber plate and the moving air, the solar air heater (SAH) efficiency can be improved [1,2].

The flat-plate SAH thermal efficiency (η_{th}) is decreased due to the low h value between the absorber plate and the airflow. A laminar sub-layer that forms next to the absorber surface when air passes through the duct of an SAH reduces heat transfer to the air stream and, consequently, the η_{th}. The laminar-to-turbulent conversion of the boundary layer zone is achieved by applying artificial roughness to the absorber plate on one or both sides. That leads to a rise in h values and the rate of heat transfers in the duct.

Artificial roughness can be produced on the SAH absorber surface by providing meshing or extended characters such as fines, blockages, vortex generators, tabulators, or ribs. Dimensional and geometric configurations for different types of ribs were investigated by various research scholars. The Thermo-Hydraulic Performance (THP) of an SAH is noticeably improved by multi-V shape ribs [3]. Excessive turbulence may result in higher power demands for airflow, demanding a careful selection of the roughness element and its design because the energy needed to induce turbulence comes from the blower or fan.

Arrangements such as the dimensioning optimization of ribs, gaps between ribs, staggering arrangement between gaps, and partial and full perforation in ribs reduce the friction losses and improve the mixing properties of the working fluid, resulting in the better THP of an SAH.

Double-Pass SAHs (DPSAH) considerably increase the collector surface area and therefore offer considerable gains in heat transfer [4]. Double-Pass SAHs with crossflow [5], recycling [6], and parallel flow [7,8] are the DPSAH arrangements that were utilized as the primary factors that impacted the performance. Yadav and Prasad [9] discovered that the DPPFSAH's rate of heat gain was 8–10% higher than a smooth duct. Hernández and Quinonez [10] observed that in the case of DPSAHs, parallel flow is more advantageous than counter flow because the airflow does not gain significant useful heat by circling beneath the base plate while having a large power requirement due to pressure drops.

Singh et al. [11,12] analysed the effect of perforation for a continuous rib in multi-v geometry in Single-Pass SAHs (SPSAH) and Double-Pass Parallel Flow SAHs (DPPFSAH) and observed a significant improvement because of the application of perforation. This work further extended to the analyzing the effect of variations in the open area ratio (β) and the relative roughness width (W/w) and found the optimum value of β for peak performance in SPSAHs and DPPFSAHs [13,14]. Various research on perforation, such as half and full perforation [15], hole-circularity [16–18], proportion of β, and hole positioning [19], has been conducted to examine the perforation's influence on flow behaviour. The β value and the recirculation time have shown a significant impact on SAHs' performance [20]. The impact of perforation hole-circularity in V-shaped blockages on THPP and a correlation for SAHs have been developed by Alam et al. [17].

A mathematical model for the energy and exergy analysis of SAHs was developed by Duffie and Beckman [21]. Hap and Phu conducted a series of experiments to develop mathematical modeling for the energy analysis of single-pass [22–24], double-pass [25], and multi-pass [26] SAHs and found a strong correlation between experimental and mathematical models for different roughness geometries. Hernández and Quiñonez [10] also developed an analytical model for the thermal performance of a double-pass parallel flow solar air heater (DPPFSAH) and a double-pass counter flow SAH (DPCFSAH) and observed that an increase in air velocity also improves the heat transfer rate, and the proposed expression can be used for further computational modeling. Kumar and Saini [27] developed correlations for the Nusselt number (Nu) and friction factor (f) for an SAH having dimple-impeachments on the absorber plate. An Nu and f correlation for DPSAHs with V-rib roughness was developed by Varun et al. [28]. Ravi and Saini [29] developed Nu and f correlations for counter-flow DPSAH with discrete multi-V ribs with staggering. In their exergy-based study of an SAH duct having W-ribs, Patel and Lanjewar [30] note that the relative roughness height (e/D_h) = 0.03375 and the angle of attack (α) = 60º produced the largest increase in the exergetic efficiency (η_{exg}) of the rough SAH when compared with the smooth surface, that is, 51%. An exergy analysis of an SAH with double-V incisions in twisted tape was carried out by Kumar [31]. In SAHs with broken arc-ribs with staggering sections, Meena et al. [32] and Saini et al. [8] measured the heat transmission and friction properties. Using numerical simulations for ribbed triangular SAHs, Kumar and Kumar [33] studied the performance enhancements and the correlations for the friction factors and heat transport. Kumar et al. [34]. conducted an experimental investigation of a DPSAH with multiple-C-shaped roughness on an SAH.

The above literature reveals that the application of DPPFSAHs reduces drag forces to a minimal level, which is responsible for high pumping power while having optimum thermal effectiveness [10]. The rapid air flow rate of the supplementary streams via holes created more turbulence during detachment and reattachment, which enhances the THP of SAH [20,35,36]. Although perforation in fins and the extended surface is around a decade-old concept, perforation in the ribs ($e/Dh \approx 0.043$) was newly introduced by Singh et al. [12,13], and no single work is available that can specify the effect of perforation

variations on influencing the range and optimized values of different operational and system parameters in the case of a DPPFSAH.

Previous researchers have shown a great deal of interest in the study of DPPFSAHs' thermal performance. The current work aims to focus on developing a mathematical model and conducting an analytical study of DPPFSAHs with perforated multi-V ribs as an artificial roughness to find out the effective range of the system and operating parameters for optimum thermal, effective, and exergy performances. To validate the model, a comparison between the results of the mathematical and experimental outcomes for single-pass and double-pass SAHs was also compared to the research previously conducted by the authors.

This work will provide step-by-step methodology for efficiency prediction and explains the effect of individual flow and system parameters on thermal efficiency and their effective range in different operating conditions, which will help researchers interested in this area. This study also gives a valid reason to choose different efficiencies in different working conditions and also explains why the effective efficiency criterion in thermo-hydraulic optimization has solid recommendations for calculating the efficiency of DPPFSAHs roughened with perforated multi-V ribs.

2. Experimental Setup and Model for DPPFSAH

A DPPFSAH test rig is created by ASHRAE guidelines (AHSRAE 93-77, 1977). A detailed description of the setup, fixed, and variable parameters is discussed in a previous study conducted by Singh et al. [12] of this study. Details of the operating and dimensional parameters of this study are mentioned in Tables 1 and 2.

Table 1. Values of fixed parameters considered for the DPPFSAH.

S. No.	Parameter	Value/Range
1.	No. of Pass	Two (DPPF)
2.	Type of Flow	Parallel Flow
3.	L	1.0 m
4.	W	0.3 m
5.	H	0.025 m
6.	N	1 nos.
7.	k_{ins}	0.037 W/m-K
8.	t_{ins}	0.05 m
9.	ρ	1.105 kg/m^3
10.	μ	1.865×10^{-5} kg/s-m
11.	k	0.02624 W/m-K
12.	$\tau\alpha$	0.8
12.	H_g	0.025 m
13.	β	0 for horizontal
14.	ε_P	0.92
15.	ε_g	0.88
16.	t_g	0.004 m
17.	T_a	300 K
18.	V	1.0 m/s

Table 2. Variable parameters with operational range for DPPFSAH.

Sr. No.	Parameters Notations	Range
1.	W/w	2–10 (five values)
2.	β	0.0, 0.21, 0.27, 0.31 (four values)
3.	Re	2000–18,000 (Nine Values)
4.	$\Delta T/I$	0.002–0.02 Km^2/W (Ten Values)
5.	I	600–1000 W/m^2 (Three values)

Figure 1a,b shows the Schematic and cross-sectional view of a DPPFSAH with per-forated multi-V rib roughness, while Figure 2 shows the thermal resistance circuit of the DPPFSAH.

(a)

(b)

Figure 1. (**a**) Schematic view of parallel flow SAH with perforated multi-V rib roughness and (**b**) Cross-sectional view of the DPPFSAH duct.

Figure 2. Thermal resistance circuit of the DPPFSAH.

Heat Transfer Modes and Assumptions for Boundary Condition

For a rectangular SAH duct, the primary assumptions considered for heat transfer modes include a uniform heat flux distribution on glass cover; conductive heat transfer between the glass covering, base plate, and rear surface; and convective heat transfer inside the airstream and the glass covering or base plate [28,29]. To simplify the analysis and construction of the mathematical model, assumptions for governing equations include: the flow condition is turbulent incompressible, a temperature-independent and three-dimensional flow under quasi-steady state under leak-free conditions, and a perfectly insulated test section.

3. Thermo-Hydraulic Performance of DPPFSAH

The ratio of the working fluid's rate of efficient thermal gain (Q_u) to the amount of sun irradiation (I) attained by the collector's heated surface is known as the thermal efficiency (η_{th}) of SAH [1]. It can be expressed as:

$$\eta_{th} = Q_u / (A_p \times I) \tag{1}$$

Q_u can be calculated as [37]:

$$Q_u = \left[I\,(\tau\alpha) - U_L (T_{pm} - T_a) \right] \tag{2}$$

Q_u can also be calculated by using Bliss's [38] heat removal factor (F_R) for incoming air temperature, as follows:

$$Q_u = F_R \left[I\,(\tau\alpha) - U_L \left(T_{fi} - T_a \right) \right] \tag{3}$$

Agarwal and Larson [39] define the SAH's thermal performance for ambient air as:

$$Q_u = F_o [I(\tau\alpha) - U_L (T_o - T_a)]] \tag{4}$$

The collector heat removal factor (F_0) for outlet air is the ratio of the actual to maximum feasible heat transfer rate [40] and is expressed as:

$$F_0 = \frac{mC_p}{A_p U_L} \left[\exp\left\{ \frac{F' U_L A_p}{mC_p} \right\} - 1 \right] \tag{5}$$

The SAH efficiency factor (F') is determined by dividing the actual tangible heat collection rate by the rate that would be possible if the entire absorber plate were assumed to be at input air temperature. It is calculable as follows:

$$F' = \left(1 + \frac{U_L}{h} \right) \tag{6}$$

The relation for η_{th} can be derived from Equations (1) and (6) and can be expressed as:

$$\eta_{th} = F_o \left[(\tau\alpha) - U_L \frac{(T_{fo} - T_{fi})}{I} \right] \tag{7}$$

4. System and Operational Parameters

To examine the thermal efficiency (η_{th}) and Efficiency Enhancement Factor (EEF) of the DPPFSAH with perforated multi V-ribs and to determine the optimum values of the parameters that obtain the optimum thermal efficiency, these parameters can be divided into fixed and variable categories.

4.1. Fixed Parameters

The DPPFSAH's fixed parameters are divided into two groups: fixed system parameters and fixed operational parameters. The ambient air temperature, inlet air temperature, and wind velocity are fixed operational parameters of the heater, whereas fixed system parameters include the different components of the SAH and the associated thermos-physical characteristic parameters. Table 1 shows the values of all of these parameters with units as suggested by Beckman et al. [41] and used in experimental setup by Singh et al. [12].

4.2. Variable Parameters

Variable system parameters include *W/w* and *β*, whereas variable operational parameters include flow parameters such as Re, ṁ, Δ*T/I*, and I. Δ*T/I* determines the gain in air temperature streaming out of the SAH duct and is specified as the increase in air temperature for a given degree of solar irradiance. As a result, while constructing an SAH, the temperature increase parameter is critical in determining the temperature range for a specific commercial or non-commercial application. The thermal performance of a DPPFSAH having various perforated multi-V roughened heated absorber plates has been estimated for the range of variable parameters given in Table 2.

The simple regression equations were used to evaluate the thermo-physical properties of air:

$$\mu = 1.81 * 10^{-5} * \left(\frac{T_{fm}}{293} \right)^{0.735} \text{ N/sm}^2 \tag{8}$$

$$C_p = 1006 * \left(\frac{T_{fm}}{293} \right)^{0.0155} \text{ J/kgK} \tag{9}$$

$$K = 0.0257 * \left(\frac{T_{fm}}{293} \right)^{0.086} \text{ W/mK} \tag{10}$$

$$\rho = \frac{97500}{287.045 * T_{fm}} \text{ kg/m}^3 \tag{11}$$

$$P_r = \frac{\mu * C_p}{K} \tag{12}$$

5. Steps for Efficiency Prediction of DPPFSAH

The thermal performance of a DPPFSAH with artificially roughened perforated multi-V ribs was predicted using a computer program written in MATLAB. The prediction used the correlations for *Nu* as a function of roughness and the operating parameters discussed in the previous work carried out by Singh et al. [12] and compared with results of SPSAH [13].

Step 1. During the iterative process, a fixed set of geometrical and roughness values chosen in accordance with Table 2 are used, and varying variables such as *W/w*, *β*, *Re*, Δ*T/I*, and *I* values are taken into consideration in accordance with Table 2.

Step 2. The plate area can be found as:

$$A_p = W \times L \tag{13}$$

Step 3. The air temperature at the outlet (T_{fo}) and the change in air temperature (Δ*T*) is determined through the air inlet temperature (T_{fi}), as follows:

$$\Delta T = (\Delta T / I) * I = T_{airout} - T_{ain} \quad T_{fo} = \Delta T + T_{fi} \tag{14}$$

The air's bulk mean temperature is calculated as:

$$T_{fm} = (T_{fo} + T_{fi})/2 \tag{15}$$

The mean absorber plate is calculated as:

$$T_{pm} = \left((T_{fo} + T_{fi})/2 \right) + 10 \tag{16}$$

Step 4. The top loss coefficient (U_T) is derived by the Klein [40] and Datta [42] correlation, as follows:

$$\frac{1}{U_T} = \left[\frac{\sigma \left(T_{pm}^2 + T_g^2 \right)(T_{pm} + T_g)}{\frac{1}{\varepsilon_p} + \frac{1}{\varepsilon_g} - 1} + \left(\frac{K_a (Nu)_t}{L_g} \right) \right]^{-1} + \left[\sigma \varepsilon_g \left(T_{pm}^2 + T_g^2 \right)(T_{pm} + T_g) + h_w \right]^{-1} + \frac{t_g}{k_g} \tag{17}$$

where the temperature of the glass (T_g) is calculated as [43]:

$$T_g = \left(\frac{F_1 T_{pm} + c T_a}{1 + F_1} \right)$$

where:

$$F_1 = \frac{\left[12 * 10^{-8} \left(T_a + 0.2 \ T_{pm} \right)^3 + h_w \right]^{-1} + 0.3tg}{1 \left[6 * 10^{-8} \left(\varepsilon_p + 0.028 \left(T_{pm} + 0.5 T_a \right)^3 + 0.6 L_g^{-0.2} \left\{ (T_{pm} - T_a) cos\beta \right\}^{0.25} \right]^{-1}} \tag{18}$$

and

$$Cc = \left(\left(\frac{T_s}{T_a} \right) + \left(\frac{h_w}{3.5} \right) / 1 + \left(\frac{h_w}{3.5} \right) \right) \tag{19}$$

$$T_s = 0.0522 (T_a)^{-1.5} \tag{20}$$

$$(Nu)_t = 1 + 1.44 \left[1 - \frac{1708}{R_a cos\beta} \right] \left[1 - \frac{1708 (sin 1.8\beta)^{1.6}}{R_a cos\beta} \right] + \left[\left(\frac{R_a cos\beta}{5830} \right)^{\frac{1}{3}} - 1 \right] \tag{21}$$

$$R_a = \left(\zeta g L^3 g \Delta T / v\alpha \right) \tag{22}$$

where ζ is the volumetric coefficient of expansion, $1/K$, computed as [42]:

$$\zeta = \frac{1}{\left[\frac{(T_{fo} + T_{fi})}{2} \right]} \tag{23}$$

where g—Gravitational constant, m/s^2; ΔT—temperature differential, K; υ—kinematic viscosity, m^2/s; Ra—the Rayleigh number; and α—thermal diffusivity, m^2·s^{-1}.

Step 5. The back loss coefficient (U_B) is the ratio of thermal-conductivity (k_{ins}) and thickness (t_{ins}) of insulation [44]:

$$U_B = \frac{k_{ins}}{t_{ins}} \tag{24}$$

Step 6. The edge loss coefficient (U_E) is calculated using the collector area (A_c), insulator thermal conductivity (k_{ins}), and thickness (t_{ins}) as inputs, given as in [44].

Finally,

$$U_L = U_T + U_B + U_E \tag{25}$$

Step 7. The useful heat in duct is calculated as:

$$Q_{u1} = \left[I (\tau \alpha) - U_L (T_{pm} - T_a) \right] A_p \tag{26}$$

For the DPPFSAH, the *Re* value is determined as:

$$Re = \rho V D / \mu \tag{27}$$

Step 8. For the SPSAH and DPPFSAH, the Nu is determined by using empirical correlation developed by Singh et al. [12,14].

For an SPSAH:

$$Nu = 0.0324\, Re^{0.9648}(\beta)^{0.2338} Exp\left[1E^{-12}\,(Ln(\beta))^2\right]\left(\frac{W}{w}\right)^{0.102} Exp\left[-3E^{-14}\left(Ln\left(\frac{W}{w}\right)\right)^2\right] \qquad (28a)$$

For a DPSAH:

$$Nu = 0.0769\, Re^{0.8953}(\beta)^{0.2417} Exp\left[2E^{-13}\,(Ln(\beta))^2\right]\left(\frac{W}{w}\right)^{0.1244} Exp\left[7E^{-15}\left(Ln\left(\frac{W}{w}\right)\right)^2\right] \qquad (28b)$$

Step 9. The h value is determined by using the Nu in step 9 using the calculation given below [45]:

$$h = Nu\, k/D \qquad (29)$$

D is the hydraulic diameter in meters, which is derived using the formula:

$$D = (4(WH)/2W + 2H) \qquad (30)$$

Step 10. The plate efficiency factor is determined as [42]:

$$F' = (h/h + U_L) \qquad (31)$$

Step 11. The heat removal factor is calculated as follows [42]:

$$F_0 = \frac{mC_p}{A_p U_L}\left[\exp\left\{\frac{F' A_p U_L}{mC_p}\right\} - 1\right] \qquad (32)$$

Step 12. The useful heat gain (Q_{u2}) per unit area of the collector calculated as [37]:

$$Q_{u2} = A_p F_o\left[I(\tau\alpha) - U_L\left(T_{fo} - T_{fi}\right)\right] \qquad (33)$$

Step 13. By using steps 7 and 12, Q_{u1} and Q_{u2} are calculated and compared. If the predicted values of these two terms are not near enough, i.e., $\frac{Q_{u1} - Q_{u1}}{Q_{u1}} > 0.1\%$, then the next mean temperature (T_{pm}) of the absorber plate is revised as:

$$T_{pm} = Ta + \left[\frac{I(\tau\alpha) - \frac{Q_{u2}}{Ap}}{U_L}\right] \qquad (34)$$

Step 14. Equation (34) uses the value of T_{pm} derived in Equation (16), and the computations are repeated from step 5 to step 14. Q_{u1} and Q_{u2} have been iterated until they are near enough, i.e., ($Q_{u1} - Q_{u2} < 0.1\%$ of Q_{u1}).

Step 15. The roughened double-pass SAH's η_{th} is calculated as:

$$\eta_{th} = (Q_u / I * Ap) \qquad (35)$$

Q_u is the average heat gain, which is calculated as:

$$Q_u = ((Q_{u1} + Q_{u2})/2) \qquad (36)$$

Step 16. The f value for a DPPFSAH is determined by using the correlation developed by Singh et al. [12,14], which is presented below.

For an SPSAH:

$$f = 1.6608\, Re^{-0.529}(\beta)^{-0.2826}\, Exp\left[-2E^{-13}(Ln(\beta))^2\right]\left(\frac{W}{w}\right)^{0.1295} Exp\left[2E^{-14}\left(Ln\left(\frac{W}{w}\right)\right)^2\right] \qquad (37a)$$

For a DPPFSAH:

$$f = 0.4234 \, Re^{-0.2964} (\beta)^{-0.3897} \, Exp\left[1\text{E}-14(Ln(\beta))^2\right] \left(\frac{W}{w}\right)^{0.1836} Exp\left[-1\text{E}-14\left(Ln\left(\frac{W}{w}\right)\right)^2\right] \tag{37b}$$

Step 17. The pressure drop $(\Delta P)_d$ in the duct is calculated as:

$$\Delta P_d = \left(4fL\rho V^2/2D\right) \tag{38}$$

Step 18. The power requirement of the blower (P_m) is calculated as:

$$P_m = (\dot{m}(\Delta P_d)/\rho) \tag{39}$$

Step 19. The thermal efficiency is calculated as:

$$\eta_{th} = F_o[(\tau\alpha) - (U_L(T_o - T_i)/I)] \tag{40}$$

Step 20. The effective efficiency, η_{eff}, is determined as:

$$\eta_{eff} = ((Q_u - (P_m/C))/IA_p) \tag{41}$$

where

$$C = \eta_t . \eta_{tr} . \eta_m . \eta_f$$

The *C* value, proposed by Corter-Piacentini [46], is 0.180 (where $\eta_f = 0.65$; $\eta_m = 0.88$; $\eta_{tr} = 0.92$; and $\eta_{th} = 0.35$).

Step 21. The mean fluid temperature (T_{fm}) is calculated as:

$$T_{fm} = \left((T_{fo} - T_{fi})/\ln\left(T_{fo}/T_{fi}\right)\right) \tag{42}$$

Step 22. The Carnot efficiency is determined as:

$$\eta_c = 1 - \left(T_a/T_{fm}\right) \tag{43}$$

Step 23. The Net exergy-flow (En) is calculated as:

$$En = IAP\eta_{th}\eta_c - P_m(1 - \eta_c) \tag{44}$$

Step 24. The Exergy-rate (E_s) associated with solar irradiation is calculated as:

$$E_s = I(1 - (T_a/T_{sun})) \tag{45}$$

Step 25. The exergetic efficiency (η_{exg}) is determined as:

$$\eta_{exg} = E_n/E_s \tag{46}$$

Step 26. To cover the whole range of roughness and operating parameters as shown in Tables 1 and 2, calculations are performed from step 2 to step 25 for all possible combinations of system and operational parameters. Figure 3 shows the process-flow diagram of the computer program developed in MATLAB that performs all of the computations specified in the preceding sections.
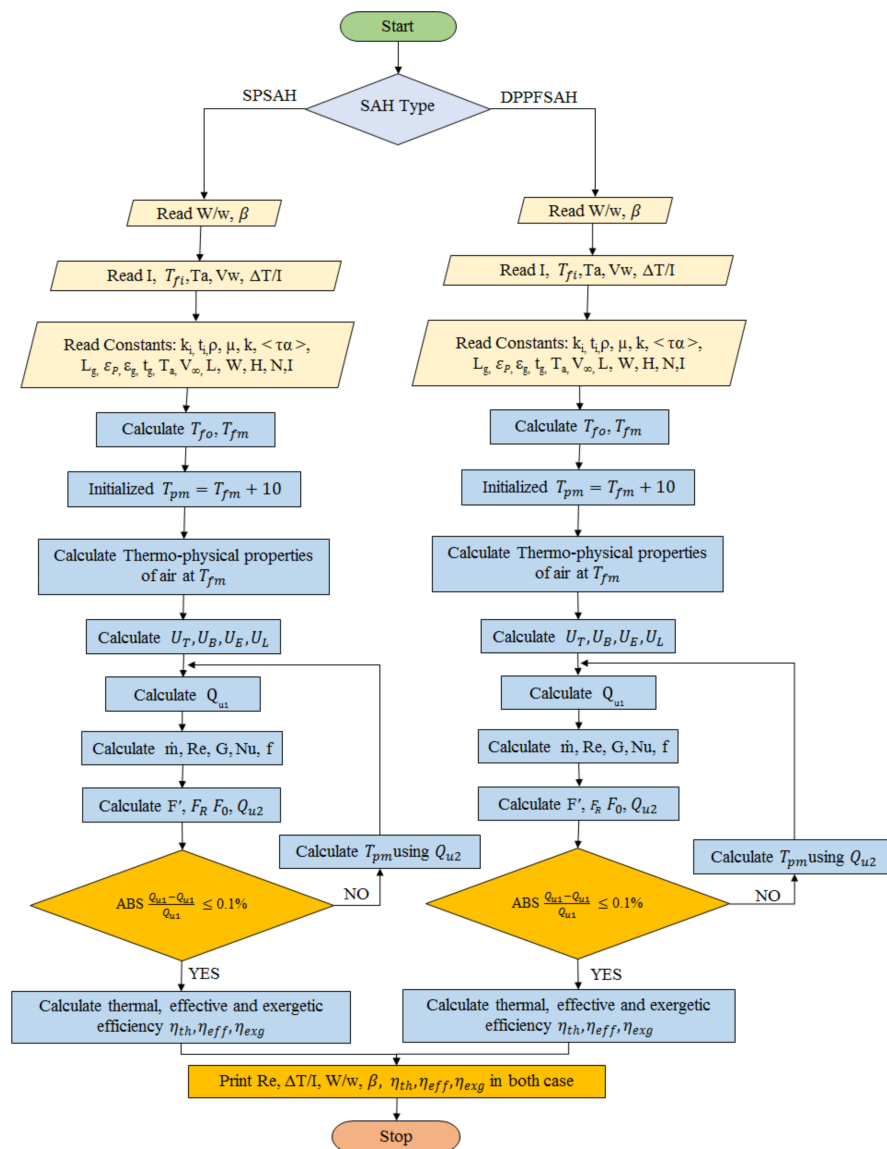
Figure 3. Flow diagram for the computer program to calculate the thermal efficiency of SPSAH and DPPFSAH.

6. Results and Discussion

The present quantitative analysis investigated the characterization of an SAH with an artificially rough surface using predefined parameters and their range, as shown in Tables 1 and 2. Plotted for the $\Delta T/I$ and Re are the findings generated for thermal, effective, and exergetic efficiencies. The heated flat plate's roughness created a second air route, reduced the reattachment zone, improved fluid blending, and improved the THP of SAH.

6.1. Effect of Flow and System Parameters on Thermal Efficiency

6.1.1. Effect of Reynolds Number (Re)

Figure 4a depicts the impact of Re on the η_{th} of a DPPFSAH roughened with varied perforated multi-V ribs for various specified roughness levels. The values of $\beta = 0.27$ and $W/w = 6$ were chosen as the optimum roughness parameters. The η_{th} of the smooth and roughened collectors increase with increase in the Re values in all instances of the SPSAH and the DPPFSAH. The improvement in the h value between the base plate and air caused by the rise in Re can be used to explain these behaviours. Roughness patterns further enhance the SPSAH's and DPPFSAH's η_{th}. In case of SPSAHs and DPPFSAHs, the

η_{th} improve from 69.66% to 80.13% and 74.74% to 86.57%, respectively, for a perforated multi-V rib roughness of $e/D = 0.043$, $\beta = 0.27$, $P/e = 10$ $\alpha = 60°$, $W/w = 6$, $W/H = 12$, and $I = 1000$ W/m^2 corresponding to an Re from 2000 to 18,000. On the other hand, for a smooth collector, the η_{th} lies between 27.66% and 65.19%, corresponding to an Re from 2000 to 18,000, respectively.
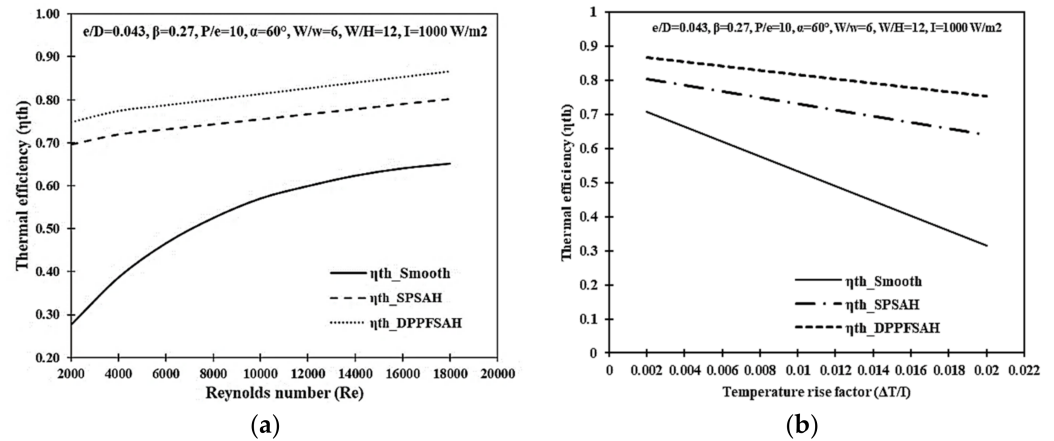

Figure 4. (**a**) η_{th} vs. Re and (**b**) η_{th} vs. $\Delta T/I$ as a function of selected values of parameters of smooth and roughened SPSAHs and DPPFSAHs.

Figure 4b shows a new plot of all the η_{th} values with a relationship of the $\Delta T/I$. As the $\Delta T/I$ increased, it was discovered that the η_{th} of the SPSAH and DPPFSAH rapidly decreased. The temperature of the entering fluid increases, the thermal gradient between the base plate and the airstream decreases. Due to this, the base plate and glass cover's average temperature increase, which increases the amount of heat lost to the environment while reducing the amount of heat gained, which is actually useful. This lowers the thermal productivity and effectiveness of the SPSAH and DPPFSAH.

6.1.2. Effect of Relative Roughness Width (W/w)

The graph of η_{th} as a function of $\Delta T/I$ for the SPSAH and the DPPFSAH is shown in Figure 5a,b. In both scenarios, the η_{th} declines and is found to be lowest at $W/w = 2$ after increasing with the increase in W/w up to 6 and then dropping with the increasing W/w values. The greatest η_{th} for both the SPSAH and the DPPFSAH was found to be 80.13% for the SPSAH and 86.57% for the DPPFSAH at $W/w = 6$ and $\beta = 0.27$.
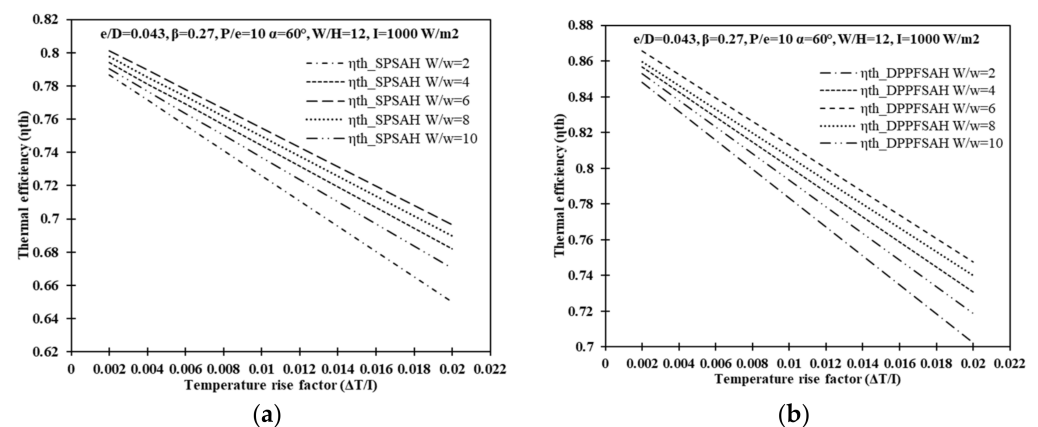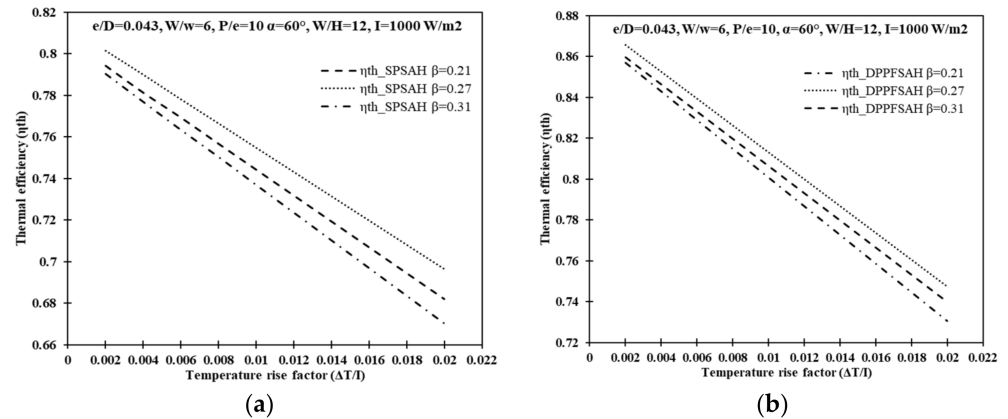

Figure 5. η_{th} vs. $\Delta T/I$ for various W/w values in (**a**) SPSAH and (**b**) DPPFSAH.

6.1.3. Effect of Open Area Ratio (β)

Figure 6a,b show that the η_{th} rises with the increase in β, reaches a maximum at 0.27, and then slightly declines as β rises further. It has been discovered that raising the β value

results in more turbulence and secondary flow mixing in the vicinity of the perforated ribs, which enhances fluid mixing and lowers the thermal barrier due to the laminar sub-layer, boosting the *h* value. In addition, as β rises over 0.27, Q_u decreases because secondary air can now be accessed through perforations, and the upper part of the rib starts to behave like a stagger, making it harder for fluid to mix effectively [20,47].


Figure 6. η_{th} vs. $\Delta T/I$ for various β values in (**a**) SPSAH and (**b**) DPPFSAH.

6.2. Efficiency Enhancement Factor (EEF)

The efficiency enhancement factor (EEF) is the ratio of the η_{th} of an SAH with and without artificial roughness operating under similar conditions:

$$\text{Efficiency Enhancement factor (EEF)} = \frac{(\eta th)_{Rough}}{(\eta th)_{Smooth}} \tag{47}$$

Figure 7a,b show the effect of W/w and β on EFF as a function of $\Delta T/I$ for a DPPFSA, and the largest and smallest EEFs for a DPPFSAH are 2.37 and 1.2, respectively.
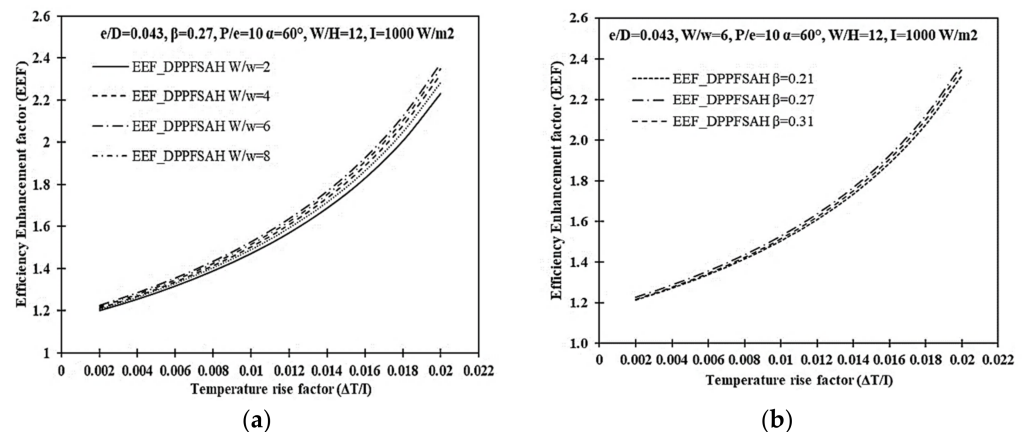
Figure 7. Effect of variation in (**a**) W/w and (**b**) β on EEF as a function of $\Delta T/I$ for DPPFSA.

6.3. Effect of Insolation on EEF

The EEF presented with the insolation levels of 600, 800, and 1000 W/m^2 have been considered. From Figure 8, it is evidently observed that the EEF increased with the rise in *I* value. In addition, as the $\Delta T/I$ increased, the EEF increases for a given value of *I*. The maximum and minimum efficiency improvement factors were found at insolation values of 1000 W/m^2 and 600 W/m^2.
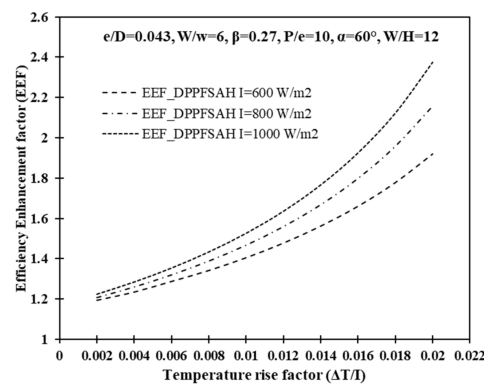
Figure 8. *EEF* vs. $\Delta T/I$ at different I values for DPPFSAH.

7. Effective Efficiency (η_{eff}) Criteria for DPPFSAH

The true effectiveness of an SAH can be expressed in terms of "η_{eff}", which accounts for the useful energy gain and equivalent heat required to generate equal mechanical energy to overcome pressure losses, as per Cortes and Piacentini [46]. For a DPPFSAH, the optimum value of η_{eff} was acheived at a W/w of 6 when the $\Delta T/I$ was more than 0.01107 Km^2/W. Similarly, for $\Delta T/I$ values less than 0.00371 Km^2/W, the DPPFSAH's smooth collectors perform better than roughened collectors in SPSAHs and DPPFSAHs. Figure 9a,b show that, for a given value of W/w, the DPPFSAH's η_{eff} improves as *Re* increases, reaches an optimum value, and then starts decreasing as the *Re* rises further. The optimum η_{eff} is found at $W/w = 6$, $Re = 8527$. The DPPFSAH roughened plate has a higher η_{eff} for *Re* greater than 19,025. As a result, it is discovered that the roughness geometry in the form of a perforated multi-V shaped rib pattern performs better at lower *Re* values. While Influence of β on η_{eff} as a function of $\Delta T/I$ and *Re* for DPPFSAH is shown in Figure 10a,b and the range of parameters β and $\Delta T/I$ for highest η_{eff} for different combination of DPPFSAH is shown in Table 3.
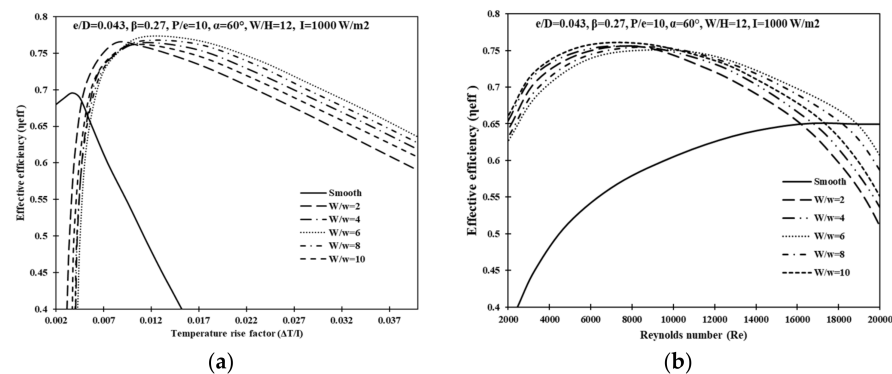

(**a**)

(**b**)

Figure 9. Influence of W/w on η_{eff} as a function of (**a**) W/w and (**b**) Re values for DPPFSAH.
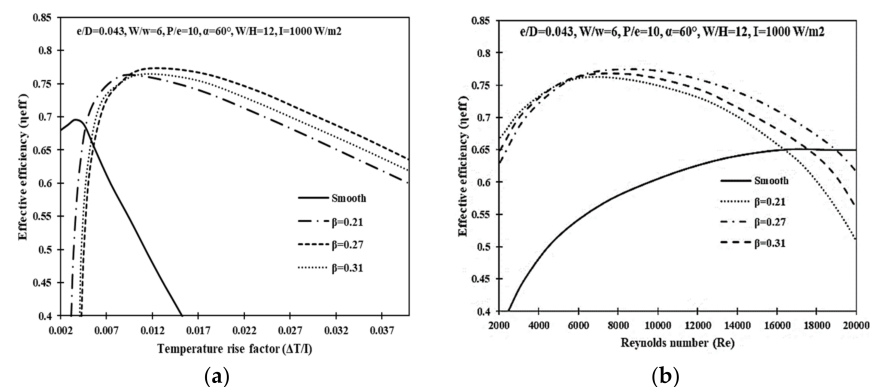

(**a**)

(**b**)

Figure 10. Influence of β on η_{eff} as a function of (**a**) $\Delta T/I$ and (**b**) Re for DPPFSAH.

Table 3. Values of β and range of Δ*T/I* for highest η_{eff} for different combination of DPPFSAH.

Geometric Parameter	Δ*T/I* (Km²/W)	β
β	0.00359 < Δ*T/I* < 0.00794	0.21
	0.01091 < Δ*T/I*	0.27
	0.00794 < Δ*T/I* < 0.01091	0.31
	Δ*T/I* < 0.00359	Smooth
Geometric Parameter	***Re***	***β***
β	Re < 5644	0.21
	5860 < Re < 18,821	0.27
	5557 < Re < 8527	0.31
	18,821 < Re	Smooth

For varying values of *Re* and Δ*T/I*, Table 4 shows the geometric parameters that correlate to the highest value of η_{eff}. System and design characteristics such as *e/D*, *β*, *p/e*, *α*, and *I* are kept constant.

Table 4. Values of Δ*T/I* for *W/w* and Re for highest η_{eff} for different combinations in DPPFSAH.

Geometric Parameter	Δ*T/I* (Km²/W)	*W/w*
W/w	0.00835 < Δ*T/I* < 0.01126	10
	0.00815 < Δ*T/I* < 0.01128	8
	0.01128 < Δ*T/I*	6
	0.00823 < Δ*T/I* < 0.01117	4
	0.00371 < Δ*T/I* < 0.01128	2
	Δ*T/I* < 0.00371	Smooth
Geometric Parameter	**Re**	***W/w***
W/w	Re < 7239	10
	8527 < Re < 8741	8
	11,881 < Re < 19,025	6
	7239 < Re < 8527	4
	5644 < Re < 8527	2
	19,025 < Re	Smooth

Geometric Parameter Optimization Using the Effective Efficiency Criteria

The optimum geometric parameter is an arrangement of geometric parameter values (*W/w*, *β*) associated with the best value of effective efficiency (η_{eff}) for a given range of design parameters (Δ*T/I*, *I*). For different values of solar radiation intensity (*I*), Figure 11a shows the variation in optimum values of *W/w* with Δ*T/I* for different values of *I*. For Δ*T/I* < 0.009572 Km²/W, the best value of *W/w* is 2 for a DPPFSAH. For a DPPFSAH, the ideal *W/w* is 6 for Δ*T/I* > 0.01128 K-m²/W for the entire range of *I*. However, the optimum value of *W/w* for a DPPFSAH is discovered to be a function of Δ*T/I* (ranging between 0.009572 K-m²/W and 0.01128 K-m²/W) and *I*. Table 5 shows a summary of the findings. While Figure 11b shows the variation of optimum values of *β* as a function of Δ*T/I* for different *I* values. The *β* = 0.21 represents the optimum settings for Δ*T/I* < 0.00794 K-m²/W for a DPPFSAH for the entire range of *I* studied. The *β* = 0.27 for Δ*T/I* > 0.01091 Km²/W reflects the best conditions for all the selected *I* values.
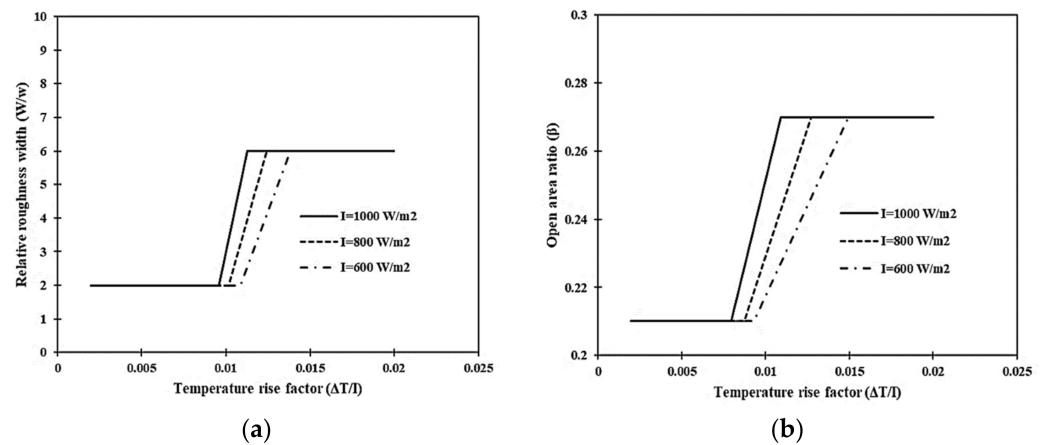
(a)

(b)

Figure 11. Optimum values of (**a**) W/w and (**b**) β for DPPFSAH.

Table 5. Range of $\Delta T/I$ and optimum W/w and β values based on η_{eff} criterion.

Geometric Parameters	$\Delta T/I$ (Km^2/W)	W/w (Optimum)
W/w	$\Delta T/I < 0.009572$ $0.009572 < \Delta T/I < 0.01058$ $0.01058 < \Delta T/I$	2 Function of $\Delta T/I$ of I 6
Geometric Parameters	**$\Delta T/I$ (Km^2/W)**	**β (Optimum)**
β	$\Delta T/I < 0.00794$ $0.00794 < \Delta T/I < 0.01091$ $0.01091 < \Delta T/I$	0.21 Function of $\Delta T/I$ of I 0.27

8. Exergetic Efficiency (η_{exg}) Criterion for DPPFSAH

Atfeld et al. [48] proposed an exergetic efficiency criterion based on the second law of thermodynamics to characterize the optimum values of geometric and operating characteristics. The value of W/w corresponding to maximal η_{exg} varies with $\Delta T/I$, as shown in Figure 12a. For a DPPFSAH, the optimum value of η_{exg} was reached at a W/w of 6, corresponding to a $\Delta T/I$ value greater 0.15298 Km^2/W, respectively. The smooth DPPFSAH shows a better η_{exg} compared to roughened DPPFSAH. Figure 12b depicts the variation in η_{exg} with Re for different values of W/w and fixed values of other parameters, the optimum value of η_{exg} has been obtained at $W/w = 6$ for $Re < 3685$, whereas for $Re > 9228$, the smooth DPPFSAH shows better η_{exg} compared to roughened DPPFSAH. The details of optimum range are given in Table 6.
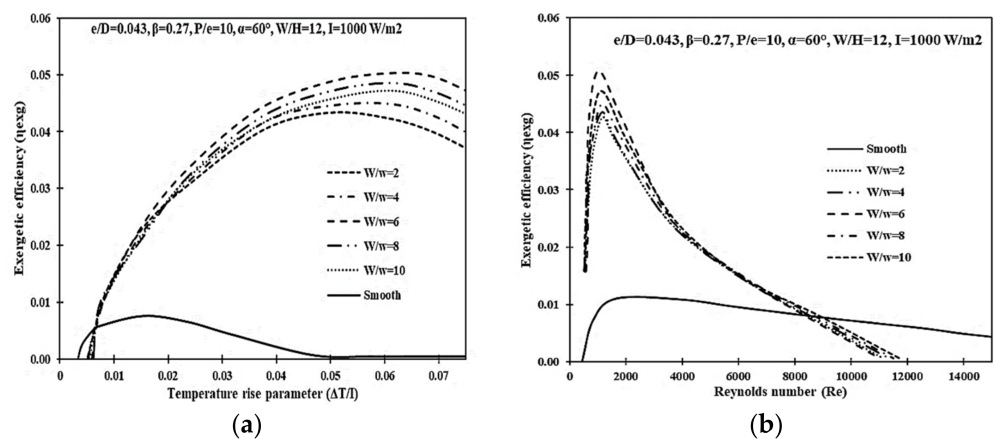

(a)

(b)

Figure 12. (**a**) η_{exg} vs. $\Delta T/I$ and (**b**) η_{exg} vs. Re graph for various W/w values for DPPFSAH.

Table 6. Range of $\Delta T/I$ and Re for different W/w corresponding to highest η_{exg} range for different combinations of DPPFSAH.

Geometric Parameter	$\Delta T/I$ (Km^2/W)	W/w
W/w	$0.05021 < \Delta T/I < 0.06134$	10
	$0.049893 < \Delta T/I < 0.06134$	8
	$0.015298 < \Delta T/I$	6
	$0.04989 < \Delta T/I < 0.06117$	4
	$0.\,0.0059 < \Delta T/I < 0.00871$	2
	$\Delta T/I < 0.006985$	Smooth
Geometric Parameter	**Re**	W/w
W/w	$605 < \text{Re} < 1075$	10
	$634 < \text{Re} < 1104$	8
	$\text{Re} < 3685$	6
	$783 < \text{Re} < 1175$	4
	$6207 < \text{Re} < 8371$	2
	$9228 < \text{Re}$	Smooth

Figure 13a demonstrates that the maximum value of η_{exg} was obtained for $\Delta T/I > 0.0169$ Km^2/W at $\beta = 0.27$, whereas the maximum value of η_{exg} for a smooth DPPFSAH were obtained for $\Delta T/I < 0.01017$ Km^2/W. The detailed range of parameters and optimum range of β are given in Table 7. Figure 13b represents the variation in η_{exg} with β as a function of Re. It is observed that the optimum value of η_{exg} for smooth DPPFSAH occurs for $Re > 8955$.
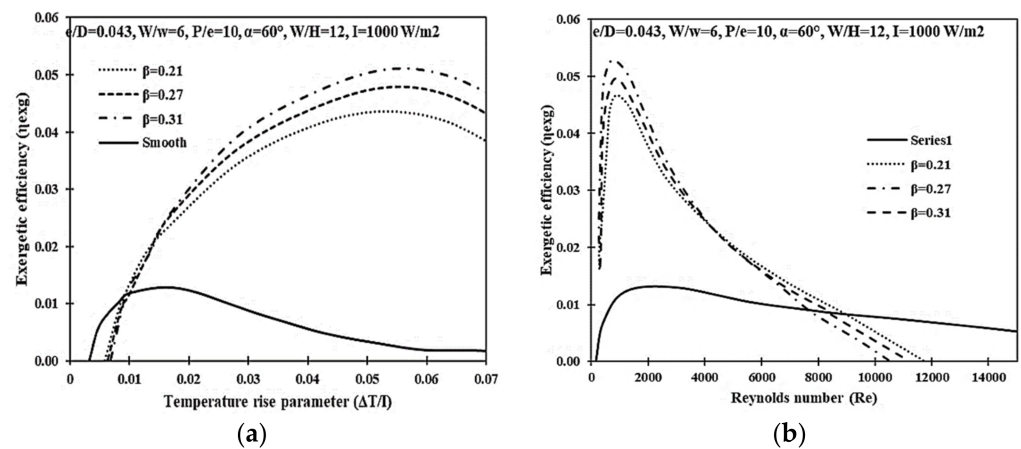
Figure 13. (**a**) η_{exg} vs. $\Delta T/I$ and (**b**) η_{exg} vs. Re relation for various β for DPPFSAH.

Table 7. Range of $\Delta T/I$ and Re for different β corresponding to the highest η_{exg} range for different combinations in DPPFSAH.

Geometric Parameter	$\Delta T/I$, Km^2/W	β
β	$0.00919 < \Delta T/I < 0.01279$	0.21
	$0.0169 < \Delta T/I$	0.27
	$0.04055 < \Delta T/I < 0.05271$	0.31
	$\Delta T/I < 0.00359$	Smooth
Geometric Parameter	**Re**	β
β	$6182 < \text{Re} < 7930$	0.21
	$\text{Re} < 4052$	0.27
	$588 < \text{Re} < 937$	0.31
	$8503 < \text{Re}$	Smooth

Geometric Parameter Optimization Using the Exergetic Efficiency (η_{exg}) Criterion

The optimum value of W/w on the basis of the highest η_{exg} has been drawn in Figure 14a for a DPPFSAH, for a given range of $\Delta T/I$. The W/w value of 2 indicates the best condition for the DPPFSAH, $\Delta T/I < 0.006051$ Km^2/W, for the entire range of I, i.e., from 600 to 1000 W/m^2. Furthermore, for all values of I, $\Delta T/I > 0.008084$ Km^2/W constitutes the optimal condition for a W/w value of 6. For a DPPFSAH, the optimum value of W/w is a function of I for $\Delta T/I$ values between 0.006051 Km^2/W and 0.008084 Km^2/W, respectively. Figure 14b depicts the optimum values of β for different values of $\Delta T/I$ and I. For the value of β of 0.21, the optimum values are obtained for $\Delta T/I$ values up to 0.00794 Km^2/W for DPPFSAH. For the values of $\Delta T/I$ above 0.01091 Km^2/W, a β value of 0.31 gives the optimum results for a DPPFSAH. However, for $\Delta T/I$ values between 0.00794 Km^2/W and 0.01091 Km^2/W, the optimum value of β is a function of I. The η_{exg} criterion plays a major role in selecting the optimum values of geometric parameters such as W/w and β based on design parameters such as $\Delta T/I$ and I, according to the above discussion. For a particular range of $\Delta T/I$ and I, a set of optimum geometric parameters can now be picked from Table 8.
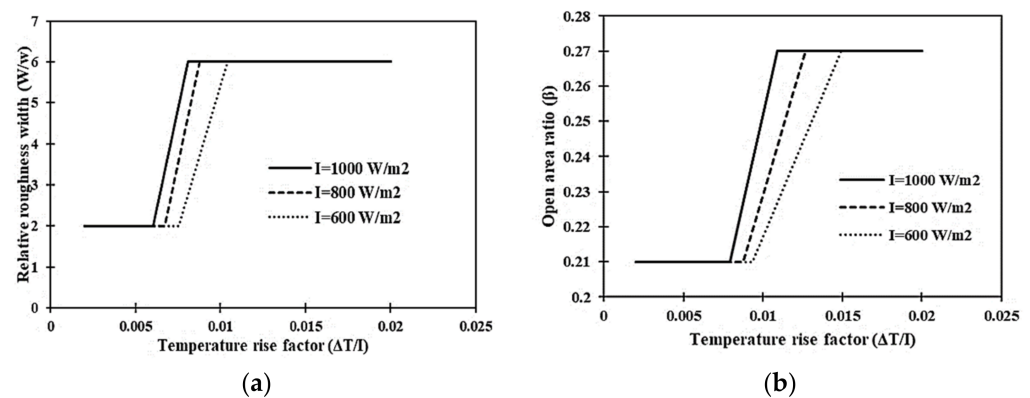

Figure 14. Optimum values of (**a**) W/w and (**b**) β for η_{exg} for DPPFSAH.

Table 8. Range of $\Delta T/I$ for optimum values of W/w and β based on η_{exg} criterion for DPPFSAH.

Rib Roughness Parameter	$\Delta T/I$ (Km^2/W)	W/w (Optimum Value)
W/w	$\Delta T/I < 0.006051$ $0.006051 < \Delta T/I < 0.008084$ $0.008084 < \Delta T/I$	2 Function of $\Delta T/I$ of I 6
Rib Roughness Parameter	**$\Delta T/I$ (Km^2/W)**	**β (Optimum Value)**
β	$\Delta T/I < 0.00827$ $0.00827 < \Delta T/I < 0.0169$ $0.0169 < \Delta T/I$	0.21 Function of $\Delta T/I$ of I 0.27

9. Comparison of Optimization Criteria

In order to maximize heat transfer while utilising the lowest amount of blowing or pumping energy, the roughness geometry must be chosen carefully. The optimal values for a group of geometric parameters can be chosen to achieve this objective. The three optimizing criteria described in this study include the η_{th}, η_{eff}, and η_{exg} criteria.

The single geometrical parameter that is optimal for all chosen values of $\Delta T/I$ is provided by the η_{th} criteria. As a conclusion, Table 9 demonstrate that the best artificial roughness geometries for a DPPFSAH is a combination of the best values of the design variables, namely, a W/w of 6 and a β of 0.27. Although no single pairing of design parameters displays the optimal values for the entire range of the $\Delta T/I$ in the case of the η_{eff} requirements and the η_{exg} standards, it is noted that no single pairing of design parameters displays the optimal values for all chosen values of the $\Delta T/I$. An artificially roughened

DPPFSAH with $\beta = 0.27$ and $W/w = 6$ outperforms all other permutations of DPPFSAHs on all three criteria.

Table 9. $\Delta T/I$ range for optimum roughness parameters as determined by the η_{eff} and η_{exg} criteria for $I = 1000 \text{ W/m}^2$.

Rib Roughness Parameter	$\Delta T/I$ (Km²/W)	Rib Roughness Parameter (Optimum Value)
W/w	$\Delta T/I < 0.006051$	2
	$\Delta T/I > 0.01128$	6
β	$\Delta T/I < 0.00794$	0.21
	$\Delta T/I > 0.01693$	0.27

The design parameters of Figure 15a,b, which show a nearly identical maximum solution for $I = 1000 \text{ W/m}^2$ generated using the η_{eff} and η_{exg} criteria, were used to calculate the range of $\Delta T/I$ given in Table 9. According to the η_{eff} and η_{exg} criteria for various amounts of solar irradiance, Table 10 illustrates the $\Delta T/I$ range where the optimal geometric parameter values vary. As shown in the analysis, the optimal values of geometric parameters depend directly on the optimization criteria employed. Therefore, selecting the factors to take into account in order to improve the desired results of SAH becomes crucial. The blower power required to move air through the collector is not included in η_{th} metrics; rather, they solely take into account gains in thermal energy. In order to maximise the performance of SAH, the thermo-hydraulic considerations, specifically η_{eff} and η_{exg}, should be applied.
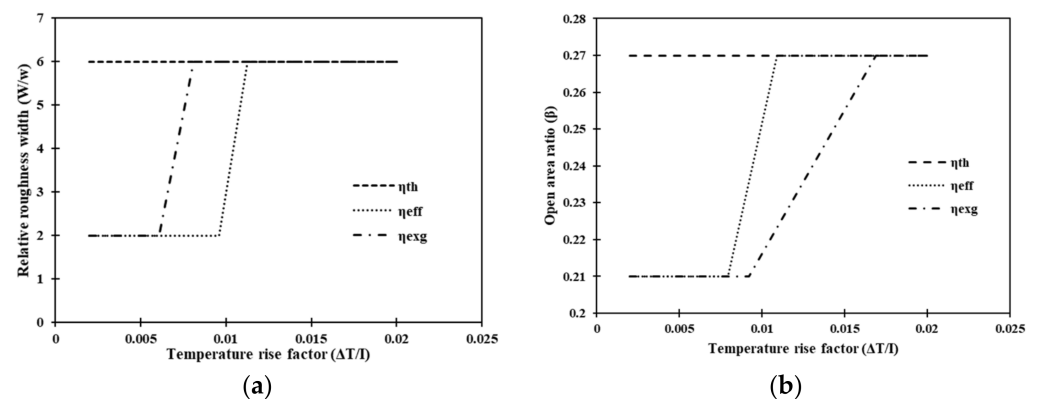
Figure 15. Comparison of optimum values of (**a**) W/w and (**b**) β for DPPFSAH.

Table 10. For varied I in DPPFSAH, the range of $\Delta T/I$ for optimum roughness parameter values are different to η_{eff} and η_{exg} requirements.

Insolation (W/m²)	Roughness Parameter	Range of $\Delta T/I$
1000	W/w	$0.006051 < \Delta T/I < 0.008084$
	β	$0.0079413 < \Delta T/I < 0.010914$
800	W/w	$0.006719 < \Delta T/I < 0.008799$
	β	$0.008753 < \Delta T/I < 0.012713$
600	W/w	$0.007528 < \Delta T/I < 0.010399$
	β	$0.009325 < \Delta T/I < 0.014937$

Only in cases where there is a thermo-hydraulic conversion of heat into work is the η_{exg} criterion applicable. Due to their narrow temperature range of operation, SAHs are not suitable for work generation. It has been demonstrated that the total exergy flow has negative values in some low-temperature uses. The η_{exg} criterion is therefore crucial when calculating thermal power at high average temperature. Additionally, the η_{eff} requirement

takes into account the rise in useable heat energy, which is constrained by the energy required to supply blowers the energy to make up for pressure losses. Thus, from the perspective of thermo-hydraulic optimization, the η_{eff} criterion has been suggested for DPPFSAHs roughened with perforated multi-V ribs.

10. Conclusions

Mathematical modeling and parametric optimization of a DPPFSAH using thermal, effective, and energetic efficiency assessments was completed for a perforated multi-V roughened base plate. As an outcome of the optimization procedure carried out for the design parameters for various operating scenarios under the assumption of η_{eff}, the optimal values are shown.

The primary conclusions drawn from the results of this study shows that the THP of the DPPFSAH is improved by perforation in multi-V rib roughness because it produces secondary passages for flowing fluids and speeds up fluid mixing. According to the analytical findings, *Re* and $\Delta T/I$ have a substantial impact on how the geometric properties of the DPPFSAH (W/w and β), influencing heat transfer efficiency. With $W/w = 6$ and $\beta = 0.27$, the optimum value of η_{th} was found to be 86.57% for rough surfaces and 74.74% for smooth ducts. For a DPPFSAH, the optimum design noted *EEF* = 2.37 at $W/w = 6$, $\beta = 0.27$ and $I = 1000$ W/m^2. The blower power is considerable at lower $\Delta T/I$ values; hence, the EEF increases as the *Re* and $\Delta T/I$ intensities increase. It is also observed that smooth collectors perform better than roughened DPPFSAH collectors for $\Delta T/I$ values below 0.00371 Km^2/W, while the best value of η_{eff} was achieved at $W/w = 6$, when $\Delta T/I$ >0.01107 Km^2/W. Similar to η_{eff}, which becomes better as *Re* rises and reaches its peak value for $W/w = 6$ at *Re* = 8527, η_{eff} then starts to fall for all W/w values as the *Re* values continue to rise. In comparison to the roughened DPPFSAH, the smooth DPPFSAH has a higher η_{eff} for an *Re* > 19,025.

For DPPFSAHs, when the $\Delta T/I$ is more than 0.01091 Km^2/W, the effect of $\Delta T/I$ on η_{eff} as a function of β attends the highest value of η_{eff} at $\beta = 0.27$, and once the $\Delta T/I$ < 0.00359 Km^2/W, the smooth collector outperforms the roughened DPPFSAH. The smooth DPPFSAH has a larger η_{eff} for an *Re* > 18,821, and the best η_{eff} is found for $\beta = 0.27$ at *Re* = 8527. The smooth DPPFSAH also demonstrates higher η_{exg} than the roughened DPFPSAH with $\Delta T/I$ < 0.006985 Km^2/W, with the optimal value of η_{exg} being attained at a $W/w = 6$ and at $\Delta T/I$ above 0.015298 Km^2/W. The maximum value of η_{exg} has been reached for *Re* < 3685 and $W/w = 6$, but for *Re* > 9228, the smooth DPPFSAH indicates a higher η_{exg} in comparison to the roughened DPPFSAH. The optimum value of η_{exg} has been obtained for $0.0169 < \Delta T/I$ K.m^2/W at $\beta = 0.27$, whereas the highest value of η_{exg} for smooth SPSAH has been obtained for $\Delta T/I$ < 0.00359 K.m^2/W. As a consequence, it is found that a perforated multi-V shaped rib patterns roughness architecture works better at smaller *Re* levels and larger $\Delta T/I$ values. The effective efficiency η_{eff} criterion was found for a DPPFSAH roughened with perforated multi-V ribs. The *Re* range of 2000–18,000 for DPPFSAH can be designed using the results of the current study.

Author Contributions: The significant contributions of authors are as follows: conceptualization: V.P.S., and S.J.; methodology: V.P.S. and S.J.; setup development: V.P.S. and S.J.; validation: V.P.S., A.K. (Ashish Karn), and C.S.M.; formal analysis of setup and testing practices: A.K. (Ashwani Kumar), G.D., A.K. (Ashish Karn), R.C., and C.S.M.; testing, investigation, and data collection: V.P.S.; resources: S.J., G.D., and C.S.M.; data curation: V.P.S. and A.K. (Ashwani Kumar); writing—original draft: V.P.S., C.S.M., and R.C.; writing—review and editing: V.P.S., S.J., C.S.M., A.K. (Ashwani Kumar), R.C., and A.K. (Ashish Karn); visualization: S.J., G.D., and C.S.M.; supervision: S.J., C.S.M., and R.C.; project administration: S.J. and R.C. All authors have read and agreed to the published version of the manuscript.

Data Availability Statement: Not applicable.

Conflicts of Interest: The authors declare no conflict of interest.

Nomenclature

Details of symbols		**Greek symbols**	
A	Area, (m^2)	Δ	Drop/gradient
C_d	Coefficient of discharge	∆	Partial
P	Mean static pressure N/m^2	η	Efficiency
H	Height, (m)	∈	Emissivity
h	Heat-transfer coefficient (W/m^2·°C)	υ	Kinematic viscosity, (m^2/s)
I	Solar Irradiance (W/m^2)	α	Absorptivity
k	Thermal conductivity (W/m°C)	σ	Stefan–Boltzmann constant (W/m^2·K^4)
t	Thickness (m)	ρ	Air density, (kg/m^3)
$\dot{m}$	Air mass-flow rate, (kg/s)	α	Angle of attack, (°)
P	Pitch distance (m)	β	Collector slope (°), Open area ratio
Q	Thermal energy transferred (J)	μ	Dynamic viscosity (N.s/m^2)
q	Average heat generation (W/m^3)	ψ	Circularity
T	Mean Temperature (°C)	ν	Kinematic viscosity m^2/s
W	Width of channel, (m)		
w	Width of one set of rib, (m)	τ	Transmissivity
V	Velocity of working fluid (m/s)	**Abbreviations**	
D_h	Hydraulic diameter (m)	DPPF	Double-Pass Parallel Flow
Subscripts		THPP	Thermohydraulic performance parameter
A	Ambient, Air		
abs	Absorber	SAH	Solar Air Heater
Amb	Ambient	m	Mean
d	Duct/ channel, diameter	u	Useful
g	Glass cover	t	Thermal
h	Height, hole	eff	Effective
Ins	Insulation	ex.	Exergetic

References

1. Klein, S.A.; Beckman, W.A.; Duffie, J.A. A design procedure for solar air heating systems. *Sol. Energy* **1977**, *19*, 509–512. [CrossRef]
2. Saini, M.; Sharma, A.; Singh, V.P.; Jain, S.; Dwivedi, G. Solar Thermal Receivers—A Review. *Lect. Notes Mech. Eng.* **2022**, *2*, 311–325. [CrossRef]
3. Alam, T.; Meena, C.S.; Balam, N.B.; Kumar, A.; Cozzolino, R. Thermo-hydraulic performance characteristics and optimization of protrusion rib roughness in solar air heater. *Energies* **2021**, *14*, 3159. [CrossRef]
4. Alam, T.; Kim, M.-H. Heat transfer enhancement in solar air heater duct with conical protrusion roughness ribs. *Appl. Therm. Eng.* **2017**, *126*, 458–469. [CrossRef]
5. Singh, S. Experimental and numerical investigations of a single and double pass porous serpentine wavy wiremesh packed bed solar air heater. *Renew. Energy* **2020**, *145*, 1361–1387. [CrossRef]
6. Ho, C.D.; Hsiao, C.F.; Chang, H.; Tien, Y.E. Investigation of Device Performance for Recycling Double-pass V-corrugated Solar Air Collectors. *Energy Procedia* **2017**, *105*, 28–34. [CrossRef]
7. Fudholi, A.; Sopian, K.; Ruslan, M.H. Thermal Efficiency of Double Pass Solar Collector with Longitudinal Fins Absorbers Thermal Efficiency of Double Pass Solar Collector with Longitudinal Fins Absorbers. *Am. J. Appl. Sci.* **2011**, *8*, 254–260. [CrossRef]
8. Kumar, A.; Akshayveer; Singh, A.P.; Singh, O.P. Efficient designs of double-pass curved solar air heaters. *Renew. Energy* **2020**, *160*, 1105–1118. [CrossRef]
9. Yadav, K.D.; Prasad, R.K. Performance analysis of parallel flow flat plate solar air heater having arc shaped wire roughened absorber plate. *Renew. Energy Focus* **2020**, *32*, 23–44. [CrossRef]
10. Hernández, A.L.; Quiñonez, J.E. Analytical models of thermal performance of solar air heaters of double-parallel flow and double-pass counter flow. *Renew. Energy* **2013**, *55*, 380–391. [CrossRef]
11. Jain, S.; Gupta, J.; Singh, V.P. Analysis of the effect of perforation in multi-v rib artificial roughened single pass solar air heater:—Part A. *Exp. Heat Transf.* **2021**, 1–20. [CrossRef]
12. Gupta, J.; Singh, V.P.; Jain, S. Performance assessment of double-pass parallel flow solar air heater with perforated multi-V ribs roughness—Part B. *Exp. Heat Transf.* **2022**, 1–18. [CrossRef]
13. Singh, V.P.; Jain, S.; Gupta, J.M.L. Analysis of the effect of variation in open area ratio in perforated multi-V rib roughened single pass solar air heater—Part A. *Energy Sources Part A Recover. Util. Environ. Eff.* **2022**, 1–20. [CrossRef]

14. Singh, V.P.; Jain, S.; Kumar, A. Establishment of correlations for the Thermo-Hydraulic parameters due to perforation in a multi-V rib roughened single pass solar air heater. *Exp. Heat Transf.* **2022**, 1–20. [CrossRef]

15. Karwa, R.; Maheshwari, B.K.K. Heat transfer and friction in an asymmetrically heated rectangular duct with half and fully perforated baffles at different pitches. *Int. Commun. Heat Mass Transf.* **2009**, *36*, 264–268. [CrossRef]

16. Kwak, J.S.; Shin, S. Effect of hole shape on the heat transfer in a rectangular duct with perforated blockage walls. *J. Mech. Sci. Technol.* **2008**, *22*, 1945–1951. [CrossRef]

17. Alam, T.; Saini, R.P.; Saini, J.S. Effect of circularity of perforation holes in V-shaped blockages on heat transfer and friction characteristics of rectangular solar air heater duct. *Energy Convers. Manag.* **2014**, *86*, 952–963. [CrossRef]

18. Bahuguna, R.; Mer, K.K.S.; Kumar, M.; Chamoli, S. Entropy generation analysis in a tube heat exchanger integrated with triple blade vortex generator inserts. *Energy Sources Part A Recover. Util. Environ. Eff.* **2021**, 1–19. [CrossRef]

19. Chamoli, S.; Thakur, N.S. Heat transfer enhancement in solar air heater with V-shaped perforated baffles. *J. Renew. Sustain. Energy* **2013**, *5*, 023122. [CrossRef]

20. Tariq, A.; Panigrahi, P.K.; Muralidhar, K. Flow and heat transfer in the wake of a surface-mounted rib with a slit. *Exp. Fluids* **2004**, *37*, 701–719. [CrossRef]

21. Duffie, J.A.; Beckman, W.A.; Winston, R.; Kreith, F. Solar Energy Thermal Processes. *Phys. Today* **1976**, *29*, 62–67. [CrossRef]

22. Phu, N.M.; Bao, T.T.; Hung, H.N.; Tu, N.T.; van Hap, N. Analytical predictions of exergoeconomic performance of a solar air heater with surface roughness of metal waste. *J. Therm. Anal. Calorim.* **2020**, *144*, 1727–1740. [CrossRef]

23. Phu, N.M.; Thao, P.B.; van Hap, N. Effective efficiency assessment of a solar air heater having baffles spaced with different successive ratios. *Case Stud. Therm. Eng.* **2021**, *28*, 101486. [CrossRef]

24. Phu, N.M.; van Hap, N. Performance Evaluation of a Solar Air Heater Roughened with Conic-Curve Profile Ribs Based on Efficiencies and Entropy Generation. *Arab. J. Sci. Eng.* **2020**, *45*, 9023–9035. [CrossRef]

25. van Hap, N.; Phu, N.M. *Heat Transfer in Double-Pass Solar Air Heater: Mathematical Models and Solution Strategy*; IntechOpen: London, UK, 2022.

26. Phu, N.M.; Tu, N.T.; van Hap, N. Thermohydraulic performance and entropy generation of a triple-pass solar air heater with three inlets. *Energies* **2021**, *14*, 6399. [CrossRef]

27. Kumar, A.; Saini, R.P.P.; Saini, J.S.S. Development of correlations for Nusselt number and friction factor for solar air heater with roughened duct having multi v-shaped with gap rib as arti fi cial roughness. *Renew. Energy* **2013**, *58*, 151–163. [CrossRef]

28. Sharma, A.; Bharadwaj, G.; Varun. Heat transfer and friction factor correlation development for double-pass solar air heater having V-shaped ribs as roughness elements. *Exp. Heat Transf.* **2017**, *30*, 77–90. [CrossRef]

29. Ravi, R.K.; Saini, R.P. Nusselt number and friction factor correlations for forced convective type counter flow solar air heater having discrete multi V shaped and staggered rib roughness on both sides of the absorber plate. *Appl. Therm. Eng.* **2018**, *129*, 735–746. [CrossRef]

30. Patel, S.S.; Lanjewar, A. Exergy based analysis of solar air heater duct with W-shaped rib roughness on the absorber plate. *Arch. Thermodyn.* **2019**, *40*, 21–48. [CrossRef]

31. Kumar, B.; Patil, A.K.; Jain, S.; Kumar, M. Effects of Double V Cuts in Perforated Twisted Tape Insert: An Experimental Study. *Heat Transf. Eng.* **2020**, *41*, 1473–1484. [CrossRef]

32. Raj, B.P.; Meena, C.S.; Agarwal, N.; Saini, L.; Hussain Khahro, S.; Subramaniam, U.; Ghosh, A. A review on numerical approach to achieve building energy efficiency for energy, economy and environment (3e) benefit. *Energies* **2021**, *14*, 4487. [CrossRef]

33. Kumar, R.; Kumar, A.; Goel, V. Performance improvement and development of correlation for friction factor and heat transfer using computational fluid dynamics for ribbed triangular duct solar air heater. *Renew. Energy* **2019**, *131*, 788–799. [CrossRef]

34. Gupta, B.; Manikpuri, G.P.; Waiker, J.K.; Pandya, M. Experimental Investigation of Double Pass Solar Air Heater using different type of Porous Media. *Int. J. Curr. Eng. Technol.* **2013**, *3*, 2006–2009.

35. Alam, T.; Kim, M.-H. A critical review on artificial roughness provided in rectangular solar air heater duct. *Renew. Sustain. Energy Rev.* **2017**, *69*, 387–400. [CrossRef]

36. Meena, C.S.; Raj, B.P.; Saini, L.; Agarwal, N. Performance Optimization of Solar-Assisted Heat Pump System for Water Heating Applications. *Energies* **2021**, *14*, 3534. [CrossRef]

37. Klein, S.A.; Duffie, J.A.; Beckman, W.A. Transient considerations of flat-plate solar collectors. *J. Eng. Gas Turbines Power* **1974**, *96*, 109–113. [CrossRef]

38. Bliss, R.W. The derivations of several 'Plate-efficiency factors' useful in the design of flat-plate solar heat collectors. *Sol. Energy* **1959**, *3*, 55–64. [CrossRef]

39. Agarwal, V.K.; Larson, D.C. Calculation of the top loss coefficient of a flat-plate collector. *Sol. Energy* **1981**, *27*, 69–71. [CrossRef]

40. Klein, S.A. Calculation of flat-plate collector loss coefficients. *Sol. Energy* **1975**, *17*, 79–80. [CrossRef]

41. Beckman, W.; Bugler, J.; Cooper, P.; Duffie, J.; Dunkle, R.; Glaser, P.; Horigome, T.; Howe, E.; Lawand, T.; Van Der Mersch, P.; et al. Units and symbols in solar energy. *Sol. Energy* **1978**, *21*, 65–68. [CrossRef]

42. Garg, H.P.; Datta, G. The top loss calculation for flat plate solar collectors. *Sol. Energy* **1984**, *32*, 141–143. [CrossRef]

43. Akhtar, N.; Mullick, S.C. Approximate method for computation of glass cover temperature and top heat-loss coefficient of solar collectors with single glazing. *Sol. Energy* **1999**, *66*, 349–354. [CrossRef]

44. Mullick, S.C.; Nanda, S.K. An improved technique for computing the heat loss factor of a tubular absorber. *Sol. Energy* **1989**, *42*, 1–7. [CrossRef]

45. Kumar, S.; Mullick, S.C. Wind heat transfer coefficient in solar collectors in outdoor conditions. *Sol. Energy* **2010**, *84*, 956–963. [CrossRef]

46. Cortes, A.; Piacentini, R. Improvement of the Efficiency of a Bare Solar Collector by Means of Turbulence Promoters. *Appl. Energy* **2000**, *36*, 253–261. [CrossRef]

47. Shetty, S.P.; Paineni, A.; Kande, M.; Madhwesh, N.; Sharma, N.Y.; Karanth, K.V. Experimental investigations on a cross flow solar air heater having perforated circular absorber plate for thermal performance augmentation. *Sol. Energy* **2020**, *197*, 254–265. [CrossRef]

48. Altfeld, K. Second law optimization of flat-plate solar air heaters Part I: The concept of net exergy flow and the modeling of solar air heaters. *Sol. Energy* **1988**, *41*, 127–132. [CrossRef]